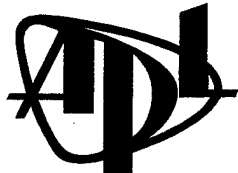


High-Frequency Bistatic Scattering Model for Elastic Seafloors

by Darrell R. Jackson

Technical Memorandum
APL-UW TM 2-00
February 2000



Applied Physics Laboratory University of Washington
1013 NE 40th Street Seattle, Washington 98105-6698

ONR Contract N00014-98-1-0119

20000218 049

ACKNOWLEDGMENTS

This work was supported by the Office of Naval Research (Program Manager Jeffrey Simmen, Code 321OA) under ONR Grant N0014-98-1-0119. The author benefitted from information provided by Dr. Eric Thorsos regarding the small-slope approximation and by Dr. Kevin Williams regarding seafloor scattering.

CONTENTS

1. INTRODUCTION	1
2. Model Input Parameters	4
2.1 Parameters Describing Average Seafloor Properties	4
2.2 Parameters Describing Roughness of Water-Seafloor Interface	5
2.3 Parameters Describing Inhomogeneity of Seafloor	5
2.4 Default Parameters for Sands, Silts, and Clays	7
3. Acoustic Definitions	10
3.1 Bistatic Scattering Strength	10
3.2 Plane Waves	11
3.3 Reflection and Transmission Coefficients	12
4. Small-Slope Approximation	14
5. Volume Scattering	17
6. Model Illustrations	19
6.1 Rough Rock	20
6.2 Rock	21
6.3 Cobble	24
6.4 Sandy Gravel	26
6.5 Coarse Sand	28
6.6 Medium and Fine Sand	30
6.7 Silt	33
7. Conclusions	36
8. References	37

LIST OF FIGURES

Figure 1. Comparison of backscattering strengths predicted by the APL-UW backscattering and bistatic scattering models for the extreme seafloor types categorized as rough rock, rock, cobble, and sandy gravel	2
Figure 2. Comparison of backscattering strengths predicted by the APL-UW backscattering and bistatic scattering models for the common seafloor types categorized as coarse sand, medium sand, fine sand, and silt	2
Figure 3. Geometry relevant to bistatic scattering from a transversely isotropic seafloor	10
Figure 4. Comparison of predictions by the elastic and fluid scattering strength models and reflection loss model for backscattering at 20 kHz from rough rock	20
Figure 5. Comparison of predictions by the elastic and fluid bistatic scattering models at 30 kHz and a 10° incident grazing angle for rough rock	21
Figure 6. Comparison of predictions by the elastic and fluid bistatic scattering models at 30 kHz and a 45° incident grazing angle for rough rock	22
Figure 7. Comparison of predictions by the elastic and fluid scattering strength models and reflection loss model for backscattering at 20 kHz from rock	22
Figure 8. Comparison of predictions by the elastic and fluid bistatic scattering models at 30 kHz and a 10° incident grazing angle for rock	23
Figure 9. Comparison of predictions by the elastic and fluid bistatic scattering models at 30 kHz and a 45° incident grazing angle for rock	23
Figure 10. Comparison of predictions by the elastic and fluid scattering strength models and reflection loss model for backscattering at 20 kHz from cobble	24
Figure 11. Comparison of predictions by the elastic and fluid bistatic scattering models at 30 kHz and a 10° incident grazing angle for cobble	25
Figure 12. Comparison of predictions by the elastic and fluid bistatic scattering models at 30 kHz and a 45° incident grazing angle for cobble	25
Figure 13. Comparison of predictions by the elastic and fluid scattering strength models and reflection loss model for backscattering at 20 kHz from sandy gravel	26

Figure 14. Comparison of predictions by the elastic and fluid bistatic scattering models at 30 kHz and a 10° incident grazing angle for sandy gravel ..	27
Figure 15. Comparison of predictions by the elastic and fluid bistatic scattering models at 30 kHz and a 45° incident grazing angle for sandy gravel ..	27
Figure 16. Comparison of predictions by the elastic and fluid scattering strength models and reflection loss model for backscattering at 20 kHz from coarse sand	28
Figure 17. Comparison of predictions by the elastic and fluid bistatic scattering models at 30 kHz and a 10° incident grazing angle for coarse sand ..	29
Figure 18. Comparison of predictions by the elastic and fluid bistatic scattering models at 30 kHz and a 45° incident grazing angle for coarse sand ..	29
Figure 19. Comparison of predictions by the elastic and fluid scattering strength models and reflection loss model for backscattering at 20 kHz from medium sand	30
Figure 20. Comparison of predictions by the elastic and fluid scattering strength models and reflection loss models for backscattering at 20 kHz from fine sand	31
Figure 21. Comparison of predictions by the elastic and fluid bistatic scattering models at 30 kHz and a 10° incident grazing angle for medium sand ..	31
Figure 22. Comparison of predictions by the elastic and fluid bistatic scattering models at 30 kHz and a 45° incident grazing angle for medium sand ..	32
Figure 23. Comparison of predictions by the elastic and fluid bistatic scattering models at 30 kHz and a 10° incident grazing angle for fine sand	32
Figure 24. Comparison of predictions by the elastic and fluid bistatic scattering models at 30 kHz and a 45° incident grazing angle for fine sand	33
Figure 25. Comparison of predictions by the elastic and fluid scattering strength models and reflection loss model for backscattering at 20 kHz from silt	34
Figure 26. Comparison of predictions by the elastic and fluid bistatic scattering models at 30 kHz and a 10° incident grazing angle for silt	34
Figure 27. Comparison of predictions by the elastic and fluid bistatic scattering models at 30 kHz and a 45° incident grazing angle for silt	35

ABSTRACT

A model for bistatic acoustic scattering at high frequencies (10–100 kHz) from elastic seafloors is developed by combining the elastic small-slope roughness scattering model of Yang and Broschat with the elastic volume scattering model of Ivakin. The combined model is applicable to a variety of seafloors, including clays, silts, sands, gravel, and rock. Although elastic effects are negligible in sands and finer sediments, they are essential in treating reflection and scattering by rock, which cannot be usefully represented by a fluid model. Use of the small-slope approximation makes it possible to avoid the cumbersome interpolation between the Kirchhoff and perturbation approximations employed in the previous APL-UW scattering models and allows larger levels of roughness than are permitted with conventional scattering approximations. The model results agree with those of the APL-UW backscattering model and with those of the APL-UW bistatic model for clays, silts, and sands. The inclusion of elastic effects attributes the high levels of scattering observed for cobble and rock seafloors to a combination of roughness and volume scattering, and replaces the empirical treatment of cobble and rock seafloors previously used in the APL-UW backscattering model by a physical one. For these cases, the new model sometimes produces unphysical results for scattering near the specular direction, indicating the need for further work on this problem.

1. INTRODUCTION

The APL-UW high-frequency acoustic models document [1] contains models for seafloor reflection, backscattering, and bistatic scattering. These models are eclectic combinations of models found in the literature, and all treat the seafloor material as a fluid. The reflection model uses the flat-interface Rayleigh reflection coefficient, while backscattering is described by a combination of four methods: the Kirchhoff approximation, the composite roughness approximation, an empirical formula for large roughness, and a semiempirical treatment of sediment volume scattering. The bistatic model [1] uses a combination of three models: perturbation theory and the Kirchhoff approximation for roughness scattering, and volume perturbation theory for sediment volume scattering. The backscattering and bistatic models have been successful in describing experimental data from a wide class of seafloor types [2–8], but certain shortcomings are evident. The most obvious problem is that the fluid approximation is very poor for rocky seafloors, where shear-wave effects become important [9–11]. A related difficulty is that the Rayleigh reflection coefficient for the two-fluid interface is known to be a bad approximation for rock [12]. As backscatter is a special case of bistatic scattering, it is possible to compare the predictions of the APL-UW backscatter and bistatic models directly. Figure 1 shows that the two models yield substantially different results for rougher seafloors, for which the APL-UW backscattering model uses an empirical fit and the bistatic model does not. Figure 2 shows that the models are very similar for sandy and silty seafloors. The differences at small grazing angles are due to the use of composite-roughness averaging in the backscatter model.

This report describes a single model that treats both backscattering and bistatic scattering for a wide range of seafloor types. This model combines two recent developments in the theory of scattering by random elastic media. These newer methods promise to alleviate some, if not all, of the problems just mentioned while providing a more streamlined formalism that is less ad hoc and empirical. This model is essentially equivalent to the older models in the regime where the latter are believed to be physically meaningful. Success outside this regime cannot be judged at present owing to a lack of suitable acoustic and physical data; however, there is no doubt that the physical basis of the new model is stronger than that of the old.

For scattering by seafloor roughness, the new model uses the small-slope formalism of Voronovich [13] as adapted to elastic seafloors by Yang and Broschat [9] and Wurmser [14]. For seafloor volume scattering, the elastic perturbation approximation developed by Ivakin [16] is used in the form outlined and extended by Ivakin and Jackson [11, 12]. These approximations will be applied to a wide variety of seafloor types and to all angles, avoiding the interpolation required in the older models mentioned previously. It should be realized that the regimes of accuracy of these newer

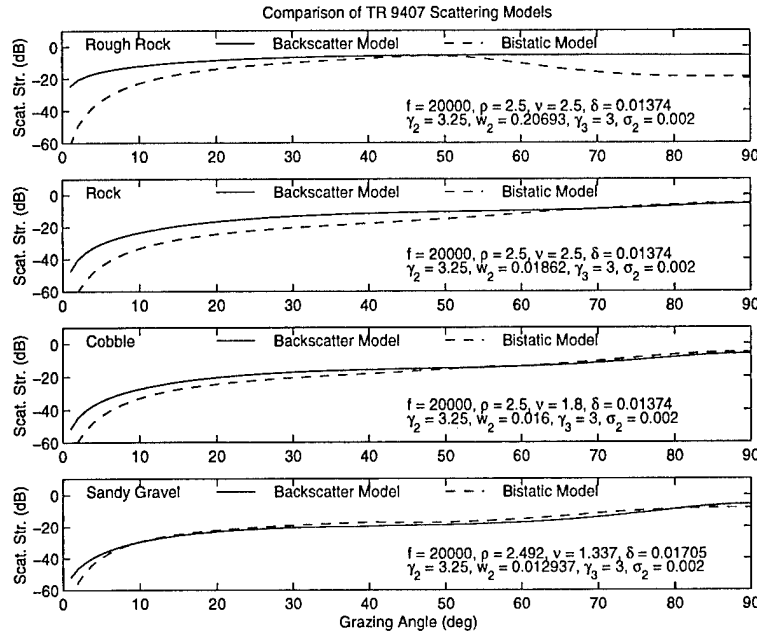


Figure 1: Comparison of backscattering strengths predicted by the APL-UW backscattering and bistatic scattering models for the extreme seafloor types categorized as rough rock, rock, cobble, and sandy gravel.

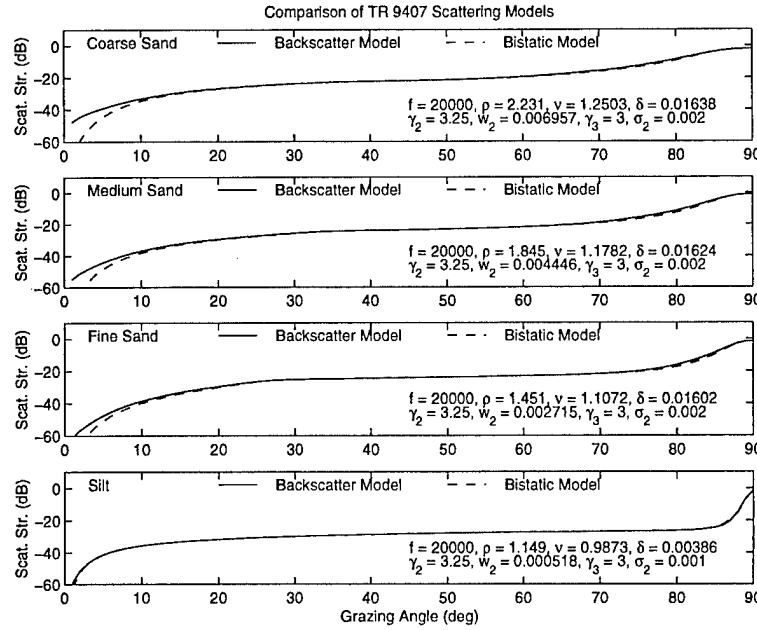


Figure 2: Comparison of backscattering strengths predicted by the APL-UW backscattering and bistatic scattering models for the common seafloor types categorized as coarse sand, medium sand, fine sand, and silt.

methods have not yet been determined. Both numerical calculations using "exact" codes and experimental data are needed to settle such issues.

The organization of this report is as follows: Section 2 defines the environmental parameters that serve as model inputs. These adhere as closely as possible to the inputs of the earlier models, although the inclusion of shear effects necessarily increases the number of parameters. Section 3 gives essential acoustic definitions, Section 4 gives formulas for the roughness scattering part of the model, and Section 5 gives formulas for the volume scattering part. Numerical illustrations are provided in Section 6, including comparisons with older models. Finally, Section 7 contains conclusions.

2. MODEL INPUT PARAMETERS

The model input parameters can be broken into three subsets: those describing the average properties of the seafloor material, those describing the roughness of the interface between the water and the seafloor, and those describing the inhomogeneity of the seafloor material. To provide the maximum level of generality allowed by the present understanding of acoustic scattering by the seafloor, the number of model parameters has been deliberately allowed to be rather large, with a total of 16 parameters. In most applications, six of these parameters can be assigned simple default values. In sands, silts, and clays, two additional parameters specifying elastic properties can be set to fixed defaults, leaving eight parameters for most applications. Even this number is too large except where considerable effort has been expended to measure physical properties of the seafloor. For more typical applications, a method for obtaining “best-guess” parameter values is outlined at the end of this section. It uses tables and equations given in the APL-UW models document [1].

The model is frequency dependent; thus the acoustic frequency, f , is also an input. In addition, the model requires a value for the speed of sound, c_w , in the water immediately above the sediment, although the results depend only weakly on this parameter.

2.1 Parameters Describing Average Seafloor Properties

There are five model parameters describing the average properties of the seafloor material. It is assumed that there are no gradients in these average properties, which are parameterized by the following dimensionless ratios:

$$a_\rho = (\text{sea floor})/(\text{water}) \text{ density ratio}$$

$$\nu_p = (\text{sea floor p-wave})/(\text{water}) \text{ sound speed ratio}$$

$$\nu_t = (\text{sea floor s-wave})/(\text{water}) \text{ sound speed ratio}$$

$$\delta_p = (\text{imaginary})/(\text{real}) \text{ ratio for p-wavenumber}$$

$$\delta_t = (\text{imaginary})/(\text{real}) \text{ ratio for s-wavenumber.}$$

The subscripts “ p ” and “ t ” are used to denote compressional and shear waves, respectively. In geophysics, compressional waves are designated “ p ” waves and shear waves are designated “ s ” waves. The subscript “ t ” (for “transverse”) is used here to denote shear, as the subscript “ s ” is used to designate the scattered field. The parameters δ_p and δ_t will be referred to as “loss” parameters and are related to the corresponding

attenuation coefficients α_p and α_s (with units of dB/m) as follows:

$$\delta_p = \frac{\alpha_p \nu_p c_w \ln 10}{40\pi f} , \quad (1)$$

$$\delta_t = \frac{\alpha_t \nu_t c_w \ln 10}{40\pi f} . \quad (2)$$

It is essential that consistent units be employed. That is, if α_p is in dB/m and c_w is in m/s, f *must* be in Hz. The parameters ν_p , a_p , and δ_p are identical to the parameters ν , ρ , and δ of the older models [1]. It is reasonable to set ν_t and δ_t to zero (or, to avoid numerical difficulties, set ν_t to a value much smaller than unity) in fine-grained sediments such as sands, silts, and clays, where shear effects are negligible [11].

2.2 Parameters Describing Roughness of Water-Seafloor Interface

The roughness parameters are identical to those employed in earlier fluid-sediment versions of this model [1, 3, 4] in which the two-dimensional spectrum of roughness is taken to be of the form

$$W(K) = \frac{w_2}{K^{\gamma_2}} . \quad (3)$$

The parameter w_2 is the “roughness spectral strength” with units of $\text{m}^{4-\gamma_2}$, and the parameter γ_2 is the “roughness spectral exponent,” with values ranging from 2 to 4. In earlier models [1] this parameter was denoted γ . It is assumed that seafloor roughness statistics are isotropic and Gaussian. Isotropy is implicit in the assumed dependence of the spectrum on the magnitude, K , of the two-dimensional wavevector, \mathbf{K} . The spectrum is normalized such that its integral over a given region of K-space is equal to the roughness variance for those spectral components. The spectrum is double-sided; that is, the wave vector argument spans both positive and negative values.

2.3 Parameters Describing Inhomogeneity of Seafloor

The volume inhomogeneity parameters are similar to those used by Ivakin and Jackson [11, 12]. The density fluctuation spectrum is assumed to be of the form

$$W_{\rho\rho}(\mathbf{k}) = \frac{w_3}{[a^2(k_x^2 + k_y^2) + k_z^2 + q_0^2]^{\gamma_3/2}} . \quad (4)$$

This is the spectrum for the dimensionless ratio of density fluctuations divided by the mean density. As such it has units of m^3 , and the “volume spectral strength,”

w_3 , has units of $\text{m}^{3-\gamma_3}$. The parameter γ_3 is the “volume spectral exponent,” with values ranging from 3 to 5. Unlike the roughness spectrum, the volume spectrum is allowed to be anisotropic, with anisotropy characterized by the “aspect ratio,” a . This parameter is the ratio of the horizontal length scale of inhomogeneity to the corresponding vertical scale and is generally equal to or greater than 1 [17,18]. While the volume inhomogeneities may be anisotropic with respect to directions in a vertical plane, they are assumed to be isotropic with respect to directions in the horizontal plane; that is, they are “transversely isotropic.” As a result, the bistatic interface scattering cross section will be isotropic. The parameter q_0 sets the largest scale of the density fluctuations [11, 18]. In the examples presented here, this parameter will be assigned a frequency-dependent default value, defined in Section 2.4. Gaussian statistics need not be assumed for volume fluctuations, as the first-order perturbation approximation used here is applicable for arbitrary statistics.

In addition to fluctuations in sediment density, the model also allows fluctuations in the compressional and shear wave speeds. These fluctuations are also normalized by division by the respective means and are assumed to have the same power-law behavior as Eq. 4. These fluctuations may be correlated with the density fluctuations, with correlations described by appropriate cross spectra. These assumptions lead to the set of model parameters defined by the following equation:

$$W_{\beta\beta'}(\mathbf{k}) = a_{\beta\beta'} W_{\rho\rho}(\mathbf{k}) . \quad (5)$$

In Eq. 5, the dimensionless parameters $a_{\beta\beta'}$ define the proportionality between the density fluctuation spectrum and the other volume fluctuation spectra,

$$W_{pp}(\mathbf{k}) = \text{p-wave fluctuation spectrum}$$

$$W_{tt}(\mathbf{k}) = \text{s-wave fluctuation spectrum}$$

$$W_{p\rho}(\mathbf{k}) = (\text{p-wave})-(\text{density}) \text{ fluctuation cross spectrum}$$

$$W_{t\rho}(\mathbf{k}) = (\text{s-wave})-(\text{density}) \text{ fluctuation cross spectrum}$$

$$W_{pt}(\mathbf{k}) = (\text{p-wave})-(\text{s-wave}) \text{ fluctuation cross spectrum.}$$

This list exhausts the possible spectra in the present problem, as the cross spectra are symmetric in their subscripts; that is, $W_{\beta\beta'}(\mathbf{k}) = W_{\beta'\beta}(\mathbf{k})$. The price of including this level of generality in the model is an additional five parameters, a_{pp} , a_{tt} , $a_{p\rho}$, $a_{t\rho}$, and a_{pt} (note $a_{pp} = 1$ by definition). The parameters a_{pp} and a_{tt} must be positive, while the parameters $a_{p\rho}$, $a_{t\rho}$, and a_{pt} are positive or negative, depending on whether the corresponding fluctuations are correlated or anticorrelated. In most of the illustrations presented in this report, all five of these parameters are set to zero, as

in unconsolidated sediments normalized wave speed fluctuations are generally much smaller than normalized density fluctuations. This is a reasonable default when no information is available on wave speed fluctuations. For rough rock and rock, these parameters are assigned values adapted from Ref. [11].

2.4 Default Parameters for Sands, Silts, and Clays

This section will conclude with suggestions for the choice of model parameters when little information is available as to seafloor type. These defaults apply to the most common sediment types (sands, silts, and clays). For extreme seafloor types (rock, cobble, and gravel), it is recommended that the parameter values used for illustrative purposes later in this report be employed unless better information is available.

As a first step, the shear parameters ν_t and δ_t are assigned values that render shear effects negligible without introducing singularities into calculations. Values $\nu_t = 0.002$ and $\delta_t = 1$ are used in this report, although the only requirement is that $\nu_t \ll 1$ and that δ_t not be large compared to unity. The volume spectral parameters a_{pp} , a_{tt} , a_{pp} , a_{tp} , and a_{pt} should be set to zero, while the aspect ratio, a , should be assigned a value of unity.

The volume spectrum scale parameter, q_0 , is inversely proportional to the length scale of the largest fluctuations, and should be assigned the small, frequency-dependent value

$$q_0 = 0.001k_w , \quad (6)$$

where k_w is the acoustic wavenumber in water, defined later in Eq. 15. This default is unphysical, but avoids difficulties that arise in perturbation theory when the volume spectra approach large values as the wavevector argument approaches zero.

For the six parameters a_ρ , ν_p , δ_p , w_2 , γ_2 and w_3 , the models document [1] should be consulted for default values. It should be remembered that in Ref. [1] a_ρ is represented by the symbol ρ and that ν_p and δ_p appear without subscripts. The volume inhomogeneity exponent is set to the value

$$\gamma_3 = 3 , \quad (7)$$

which yields a volume scattering contribution that is frequency independent, provided all other model parameters are frequency independent. A formal difficulty arises with this exponent value, as it yields an infinite value for the integral of the spectrum, corresponding to an infinite density ratio variance. Thus, even if the actual spectrum follows the assumed power law over the wavenumber range of interest, it must fall off more rapidly than the third power of wavenumber at large wavenumbers (short wavelengths). If we take this cutoff to correspond to twice the acoustic wavenumber

of the highest model frequency (100 kHz), and take the lower cutoff to be the scale parameter, Eq. 6, evaluated at the lowest model frequency (10 kHz), the approximate density ratio variance is

$$\sigma_\rho^2 \cong w_3 \ln(20000) \cong 10w_3 . \quad (8)$$

As the mean density ratio lies in the range 1–2.5, fluctuations in this parameter must be much less than unity, leading to the condition

$$w_3 << 0.1 . \quad (9)$$

This condition is satisfied by all the spectral strengths used in this report (see Table 1). The values for silt and sand were obtained using the default

$$w_3 = \frac{80\delta_p\sigma_2}{\pi \ln 10(1 + \delta_p^2)^2} , \quad (10)$$

where σ_2 is the “volume parameter” used in the older models. Equation 10 can be derived from Eq. IV-69 of Ref. [1] by taking $\gamma_3 = 3$ and giving the compressional/density fluctuation parameter, μ , a value of -1 .

Table 1: Input parameters used in model/data comparisons.

Seafloor Type	Density Ratio, a_p	Comp. Speed Ratio, ν_p	Comp. Loss Parameter, δ_p	Shear Speed Ratio, ν_t	Shear Loss Parameter, δ_t	Rough. Spectral Exponent, γ_2	Rough. Spectral Strength, $(m^{4-\gamma_2})$, w_2	Rough. Spectral Exponent, γ_3	Rough. Spectral Strength, $(m^{3-\gamma_3})$, w_3
Rough Rock	2.5	2.3	0.00174	1.3	0.085	2.75	1.0×10^{-4}	3.0	2.0×10^{-4}
Rock	2.5	2.3	0.00174	1.3	0.085	2.75	2.5×10^{-4}	3.0	6.0×10^{-5}
Cobble	2.5	1.8	0.001374	1.01	0.1	3.0	2.5×10^{-4}	3.0	1.52×10^{-3}
Sandy, Grav.	2.492	1.337	0.01705	0.156	0.2	3.0	1.8×10^{-4}	3.0	3.77×10^{-4}
Crs. Sand	2.231	1.2503	0.01638	0.134	0.075	3.25	2.2×10^{-4}	3.0	3.62×10^{-4}
Med. Sand	1.845	1.1782	0.01624	0.002	1.0	3.25	1.406×10^{-4}	3.0	3.59×10^{-4}
Fine sand	1.451	1.1072	0.01602	0.002	1.0	3.25	8.6×10^{-5}	3.0	3.54×10^{-4}
Silt	1.149	0.9873	0.00386	0.002	1.0	3.25	1.64×10^{-5}	3.0	4.269×10^{-5}

3. ACOUSTIC DEFINITIONS

This section provides definitions common to the roughness- and volume-scattering components of the model.

3.1 Bistatic Scattering Strength

The bistatic scattering strength is the decibel equivalent of the bistatic scattering cross section per unit solid angle per unit surface area. The scattering cross section will be expressed as a sum of terms corresponding to scattering by interface roughness and volume inhomogeneity; consequently, the scattering strength can be written in the form

$$s(\theta_s, \phi_s, \theta_i) = 10 \log_{10}[\sigma_r(\theta_s, \phi_s, \theta_i) + \sigma_v(\theta_s, \phi_s, \theta_i)]. \quad (11)$$

The angular variables θ_s , ϕ_s , and θ_i are defined in Fig. 3.

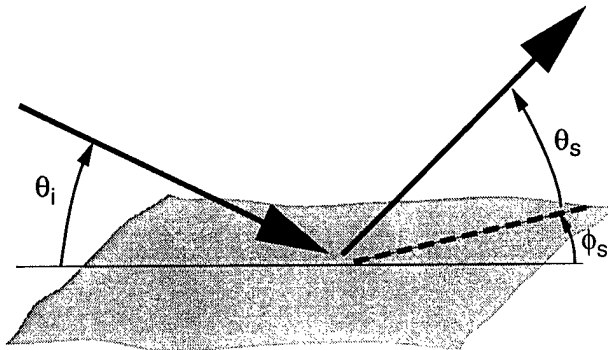


Figure 3: Geometry relevant to bistatic scattering from a transversely isotropic seafloor.

This section uses the conventions defined in Ref. [12] with slight modifications. The grazing angle of the incident acoustic energy is denoted θ_i , the grazing angle of the scattered acoustic energy is denoted θ_s , and the change in azimuth due to scattering is denoted ϕ_s . This angle will be referred to as the “bistatic angle.” In general, two azimuthal angles are needed, one for the incident energy and one for the scattered energy. However, the model assumes that roughness is isotropic and volume inhomogeneity is transversely isotropic, so that the bistatic scattering strength depends only on the difference of these two angles. Note that backscattering corresponds to the choice $\theta_s = \theta_i$, $\phi_s = 180^\circ$, and scattering in the specular direction corresponds to $\theta_s = \theta_i$, $\phi_s = 0^\circ$.

3.2 Plane Waves

Both the roughness and volume scattering components of the model employ first-order solutions of the scattering problem. In several expressions to follow, complex wave speed ratios are used. These are defined as

$$a_p = \frac{\nu_p}{1 + i\delta_p} \quad (12)$$

for compressional waves and

$$a_t = \frac{\nu_t}{1 + i\delta_t} \quad (13)$$

for shear waves.

The solutions for plane waves propagating in the upward and downward directions in a homogeneous medium can be expressed

$$\exp(i\mathbf{k}_\alpha^\pm \cdot \mathbf{r}) ,$$

where the subscript $\alpha = p$ or t and denotes the wave vector for compressional or shear waves in the seabed. The superscripts + and - denote the vertical component of phase velocity, upward and downward, respectively.

These three-dimensional wave vectors will be decomposed into transverse and vertical components and normalized by division by the wavenumber in water. That is, if we define

$$\mathbf{b}_\alpha^\pm = \mathbf{k}_\alpha^\pm / k_w , \quad (14)$$

where

$$k_w = \frac{2\pi f}{c_w} \quad (15)$$

is the wavenumber in water, the normalized wavevectors of the incident downward-propagating compressional and shear waves in the seafloor are

$$\mathbf{b}_\alpha^- = [\cos \theta_i, 0, -P_\alpha(\theta_i)] , \quad \alpha = p, t , \quad (16)$$

and the normalized wavevectors of the upward-propagating scattered waves are

$$\mathbf{b}_\alpha^+ = [\cos \theta_s \cos \phi_s, \cos \theta_s \sin \phi_s, P_\alpha(\theta_s)] , \quad \alpha = p, t . \quad (17)$$

The vertical components of the normalized wave vectors in the elastic medium are proportional to

$$P_\alpha(\theta) = \sqrt{a_\alpha^{-2} - \cos^2(\theta)} , \quad \alpha = p, t . \quad (18)$$

There are two plane-wave shear polarizations, both having particle displacement transverse to the direction of propagation. Only the shear wave having particle displacement in a vertical plane is of interest, as it is the only one that appears in the

zeroth-order problem. The particle motion for downward-propagating and upward-propagating waves is in the direction of the following dimensionless vectors

$$\mathbf{b}_v^- = [P_t(\theta_i), 0, \cos \theta_i] , \quad (19)$$

$$\mathbf{b}_v^+ = [-P_t(\theta_s) \cos \phi_s, -P_t(\theta_s) \sin \phi_s, \cos \theta_s] . \quad (20)$$

The normalization used in Eqs. (14), (16), (17), (19), and (20) differs from that used in Ref. [12], where the corresponding vectors have unit magnitude.

3.3 Reflection and Transmission Coefficients

Both the the roughness and volume-scattering portions of the model require an expression for the reflection coefficient for plane sound waves in water incident upon a flat, homogeneous elastic half-space. This reflection coefficient is [19]

$$\Gamma_w(\theta) = \frac{z(\theta) - 1}{z(\theta) + 1} , \quad (21)$$

where the normalized acoustic impedance, $z(\theta)$, is

$$z(\theta) = a_p \sin \theta \left[\frac{\cos^2 2\theta_t}{P_p(\theta)} + \frac{\sin^2 2\theta_t}{P_t(\theta)} \right] . \quad (22)$$

The variable θ_t is the complex angle of the shear wave in the seafloor material, dependent on the grazing angle in water, θ :

$$\cos 2\theta_t = 2a_t^2 \cos^2 \theta - 1 . \quad (23)$$

Equation 22 also requires

$$\sin^2 2\theta_t = 1 - \cos^2 2\theta_t \quad (24)$$

as an input. In later applications of Eqs. 21–24 the grazing angle in water, θ , will take on the value of either θ_i or θ_s . This will require double subscripting of θ_t , either θ_{ti} or θ_{ts} . The reflection coefficient is used to define the reflection loss, L ;

$$L(\theta_i) = -20 \log_{10} |\Gamma_w(\theta_i)| . \quad (25)$$

This is the reflection loss that would be measured if the seafloor were perfectly flat. Seafloor roughness will cause angular spreading, increasing loss, and will also cause time spreading.

The volume-scattering portion of the model also requires expressions for the transmission coefficients for compressional and shear waves. The transmission coefficient for the scalar potential of compressional wave particle displacement is [19]

$$\Gamma_p(\theta) = \frac{\cos 2\theta_t \sin \theta}{P_p(\theta)} [1 - \Gamma_w(\theta)] , \quad (26)$$

and the corresponding transmission coefficient for shear is [19]

$$\Gamma_t(\theta) = \frac{\sin 2\theta_t \sin \theta}{P_t(\theta)} [1 - \Gamma_w(\theta)] . \quad (27)$$

4. SMALL-SLOPE APPROXIMATION

Yang and Broschat [9] and Wurmser [14] have applied the small-slope approximation to scattering by a randomly rough interface separating two homogeneous media, one a fluid and the other a lossy elastic material. In the present model, the small-slope approximation is specialized to the isotropic case. This reduces a double integral for the bistatic scattering strength to a single integral, and further simplification results from the assumption that the coherent component of the field is zero. This is a reasonable approximation at high frequencies and was used in the predecessors to this model [1]. The resulting expression for the bistatic scattering cross section is

$$\sigma_r(\theta_s, \phi_s, \theta_i) = \frac{|A|^2}{2\pi Q^2 q_3^2} \int_0^\infty J_0(u) e^{-pu^{2\alpha}} u du , \quad (28)$$

where

$$p = \frac{1}{2} C_h^2 q_3^2 Q^{-2\alpha} , \quad (29)$$

where J_0 is the zeroth-order Bessel function of the first kind, and C_h and α are parameters of the structure function, $D(\mathbf{R})$, for two-dimensional surface roughness, $\mathbf{R} = (x, y)$. For the surfaces characterized by the power-law spectrum defined earlier, the structure function is

$$D(\mathbf{R}) = C_h^2 R^{2\alpha} \quad (30)$$

with

$$\alpha = (\gamma_2 - 2)/2 \quad (31)$$

and

$$C_h^2 = \frac{2\pi w_2 \Gamma(2 - \alpha)}{2^{2\alpha} \alpha (1 - \alpha) \Gamma(1 + \alpha)} . \quad (32)$$

The variable Q is the transverse Bragg wavenumber, the magnitude of the difference in the transverse components of the incident and scattered wavevectors.

$$Q = k_w \sqrt{\cos^2 \theta_s - 2 \cos \theta_s \cos \theta_i \cos \phi_s + \cos^2 \theta_i + b^2} . \quad (33)$$

The parameter b is assigned the value 0.001 to prevent numerical difficulties that arise if Q becomes too small. The variable q_3 is the corresponding difference in the vertical components of the incident and scattered wavevectors

$$q_3 = k_w (\sin \theta_s + \sin \theta_i) . \quad (34)$$

Equation 28 is related to the corresponding Kirchhoff and perturbation expressions. The integral in 28 is exactly the same as that used in the Kirchhoff approximation in the APL-UW bistatic model Eq. [1], the only difference being that this integral is to be used for *all* directions in the present model while its use was restricted to

near-specular directions in the previous bistatic model. It is important to note that this integral is independent of the properties of the lower medium; that is, the same integral is used for the Dirichlet (pressure release surface), Neumann (hard surface), fluid, and elastic problems. The coefficient A in Eq. 28 *does* depend on the properties of the lower medium and is obtained using first-order perturbation theory for the corresponding problem. Specifically, the bistatic cross section, $\sigma_{rp}(\theta_s, \phi_s, \theta_i)$, in first-order perturbation theory is

$$\sigma_{rp}(\theta_s, \phi_s, \theta_i) = |A|^2 W(Q) . \quad (35)$$

The coefficient, A , can be obtained for the elastic case from various sources [9, 10, 12, 20, 21]. These authors provide expressions from which A can be obtained via numerical matrix inversion. While these expressions are readily coded using high-level matrix-oriented computational tools, it is possible to obtain the required inverse analytically, yielding the following readily evaluated scalar expression for A :

$$A = \frac{k_w^2}{2} (D_1[1 + \Gamma_w(\theta_s)][1 + \Gamma_w(\theta_i)] + D_2[1 - \Gamma_w(\theta_s)][1 + \Gamma_w(\theta_i)] \\ + D_3[1 + \Gamma_w(\theta_s)][1 - \Gamma_w(\theta_i)] + D_4[1 - \Gamma_w(\theta_s)][1 - \Gamma_w(\theta_i)]) , \quad (36)$$

where $\Gamma_w(\theta)$ is the reflection coefficient defined in Eq. 21 and the variables D_n are

$$D_1 = -1 + S + \frac{1}{a_p^2 a_\rho \cos 2\theta_{ts} \cos 2\theta_{ti}} \\ - \frac{a_t^2 [(a_t^{-2} - 2 \cos^2 \theta_s - 2 \cos^2 \theta_i + 2S)S + 2 \cos^2 \theta_s \cos^2 \theta_i]}{a_p \cos 2\theta_{ts} \cos 2\theta_{ti}} , \quad (37)$$

$$D_2 = -\frac{4a_t^4 \sin \theta_s P_t(\theta_s)}{\cos 2\theta_{ts} \cos 2\theta_{ti}} [P_p^2(\theta_i) \cos^2 \theta_s + (\cos^2 \theta_i - S)S] , \quad (38)$$

$$D_3 = -\frac{4a_t^4 \sin \theta_i P_t(\theta_i)}{\cos 2\theta_{ts} \cos 2\theta_{ti}} [P_p^2(\theta_s) \cos^2 \theta_i + (\cos^2 \theta_s - S)S] , \quad (39)$$

$$D_4 = \frac{2a_t^6 a_\rho \sin \theta_s \sin \theta_i P_t(\theta_s) P_t(\theta_i)}{\cos 2\theta_{ts} \cos 2\theta_{ti}} [2(a_t^{-2} - 2S)S - 4 \cos^2 \theta_s \cos^2 \theta_i (1 - 2a_t^2 a_p^{-2})] \\ - (a_\rho - 1) \sin \theta_s \sin \theta_i . \quad (40)$$

The variable S is

$$S = \cos \theta_s \cos \theta_i \cos \phi_s . \quad (41)$$

These expressions have not been published elsewhere but are mathematically equivalent to results given by the authors cited above. The expression for A is cast in a form

similar to that used by Moe and Jackson [15], in which the flat-interface reflection coefficient, $\Gamma_w(\theta)$, appears prominently. This expression is obviously invariant under the reciprocity transformation, in which the incoming and outgoing wavevectors are interchanged after a sign reversal. In the present context, reciprocity implies that the scattering cross section be unchanged in value by the interchange of θ_i and θ_s . This invariance must be obeyed on fundamental grounds and, although it is also obeyed by the matrix expressions given in the references cited above, this symmetry is not obvious upon inspection of any of those references except Wurmser [14].

5. VOLUME SCATTERING

Ivakin [16] has treated volume scattering in shear-supporting seafloors using perturbation theory. This approach has been investigated further by Ivakin and Jackson [11, 12] who provide an expression for the apparent interface scattering cross section, $\sigma_{vp}(\theta_s, \phi_s, \theta_i)$, due to seafloor volume scattering in the perturbation approximation. Experience with this expression has shown that it sometimes predicts unrealistically large scattering cross sections near the specular direction. These values are large enough to violate energy conservation and signal a failure of the perturbation approximation. When this occurs, it is reasonable to assume that volume scattering is indeed very strong, but the actual scattering cross section will differ from that given by the model. To accommodate such situations, the volume scattering cross section, $\sigma_v(\theta_s, \phi_s, \theta_i)$, appearing in Eq. 11 will be limited to values less than the parameter, σ_0 , as follows:

$$\sigma_v(\theta_s, \phi_s, \theta_i) = [\sigma_{vp}^{-1}(\theta_s, \phi_s, \theta_i) + \sigma_0^{-1}]^{-1}. \quad (42)$$

In the examples presented in this report, the limiting scattering cross section is set to the value $\sigma_0 = 0.1$, corresponding to a maximum scattering strength of -10 dB. This value was chosen to avoid violation of energy conservation in the examples considered in this report and affects only the model results for rough rock, rock, and cobble in certain angular regimes.

The perturbation result given by Jackson and Ivakin [12] is

$$\sigma_{vp}(\theta_s, \phi_s, \theta_i) = -\frac{\pi k_w^4 a_\rho^2}{2} \operatorname{Im} \left\{ \sum_{\eta, \beta, \eta', \beta'} d_{\eta \beta} d_{\eta' \beta'}^* \frac{W_{\beta \beta'} [(\mathbf{q}_\eta + \mathbf{q}_{\eta'}^*)/2]}{(q_{\eta 3} - q_{\eta' 3}^*)} \right\}, \quad (43)$$

where Im designates the imaginary part of the complex quantity and $W_{\beta \beta'}$ is the matrix of cross spectra for volume inhomogeneities defined in Eq. 5. The argument of $W_{\beta \beta'}$ can be complex, and the resulting complex spectrum values are defined by analytic continuation of the algebraic expressions 4 and 5.

The β and β' sums run over the three types of inhomogeneity: density, compressional wave speed, and shear wave speed ($\beta, \beta' = \rho, p, t$). The η and η' sums run over the four types of wave conversion caused by volume scattering: compressional to compressional ($\eta = pp$), shear to compressional ($\eta = pt$), compressional to shear ($\eta = tp$), and shear to shear ($\eta = tt$). Thus, we can put

$$\eta = \alpha \alpha',$$

where α and α' run over the two types of waves ($\alpha, \alpha' = p, t$). The scattering vectors for the four types of conversion are

$$\mathbf{q}_\eta = k_w (\mathbf{b}_\alpha^+ - \mathbf{b}_{\alpha'}^-). \quad (44)$$

These vectors give the change in wave vector for the corresponding conversion and appear as arguments in the cross spectra in Eq. 43. The vertical components of \mathbf{q}_η are also used in Eq. 43.

$$q_{\eta 3} = k_w [P_\alpha(\theta_s) + P_{\alpha'}(\theta_i)] . \quad (45)$$

The coefficients $d_{\eta\beta}$ are

$$d_{\eta\beta} = w_\eta D_{\eta\beta} \quad (46)$$

where

$$w_\eta = \Gamma_\alpha(\theta_s) \Gamma_{\alpha'}(\theta_i) . \quad (47)$$

The coefficients $D_{\alpha\beta}$ are elements of the three-column matrix

$$D = (D_\rho | D_p | D_t) , \quad (48)$$

where $D_\rho = D'_\rho + D_t/2$ and

$$D'_\rho = \begin{pmatrix} a_p^{-2} - b_{pp} \\ b_{pv} \\ -b_{vp} \\ b_{vv} \end{pmatrix} , \quad (49)$$

$$D_p = \begin{pmatrix} 2a_p^{-2} \\ 0 \\ 0 \\ 0 \end{pmatrix} , \quad (50)$$

$$D_t = 2a_t^2 \begin{pmatrix} 2b_{pp}^2 - 2a_p^{-4} \\ -2b_{pv}b_{pt} \\ 2b_{vp}b_{tp} \\ -b_{vv}b_{tt} - b_{vt}b_{tv} \end{pmatrix} , \quad (51)$$

with

$$b_{\alpha\alpha'} = \mathbf{b}_\alpha^+ \cdot \mathbf{b}_{\alpha'}^- , \quad (52)$$

where $\alpha, \alpha' = p, t, v$, the normalized vectors \mathbf{b}_α^\pm are defined in Eqs. 16–20, and $a_v = a_t$.

6. MODEL ILLUSTRATIONS

In this section, the model will be compared with earlier backscatter and bistatic models. As the present model has several more parameters, the default parameters defined in Section 2.4 will be used to simplify the discussion. The set of parameters used to illustrate the model is listed in Table 1. These examples can be divided into three classes: (1) rough rock, rock, cobble, and sandy gravel, where roughness is large and shear effects are strong; (2) sandy sediments, where roughness is moderate but important, shear effects are small, and the sediments are “fast” (i.e., the sediment compressional wave speed exceeds the water sound speed); and (3) silt, where roughness and shear effects are negligible and the sediment is “slow” (this is also true of clay sediments). In these latter two classes, all parameters are assigned the default parameters defined earlier, except that coarse sand is given nonnegligible shear parameters taken from Ref. [11]. The parameters for rough rock and rock are adapted from the sedimentary rock example of Ref. [11], for which $a_{pp} = 9$, $a_{tt} = 16$, $a_{pp} = 3$, $a_{tp} = 4$, and $a_{pt} = 12$. This choice gives perfect correlation between density and elastic moduli. The aspect ratio, a , is assigned the value unity, departing from Ref. [11], and the spectral exponents and strengths were determined by trial-and-error fitting to the older backscatter model. For cobble and sandy gravel, no guidance is available from the literature, so the defaults $a_{pp} = a_{tt} = a_{pp} = a_{tp} = a_{pt} = 0$, and $a = 1$ were used along with trial-and-error fitting to determine the spectral exponents and strengths.

Because the backscatter model has been built upon a rather large data set and checked against data from numerous experiments, comparison of the predictions of the new bistatic model with those of the older backscatter model amounts to a comparison with data and is a crucial test. This comparison is made at a frequency of 20 kHz for bottom types ranging from rough rock to silt. Comparisons are also given between the reflection loss of the fluid model [1] and the elastic model (Eq. 25). Comparisons between the older bistatic model [1] and the present model are also made for incident grazing angles of 10° and 45° , at a frequency of 30 kHz. The bistatic scattering strength is displayed in two ways. First, for a fixed incident grazing angle, the bistatic angle is set to 180° , and the scattered grazing angle is varied from 0° to 180° (from backscattering to forward scattering). Second, the scattered grazing angle is set equal to a fixed value of the incident grazing angle, and the bistatic angle is varied from -180° to 180° . In the first case, the backscatter direction corresponds to a scattered grazing angle equal to the incident grazing angle ($\theta_s = \theta_i$), and the specular direction corresponds to $\theta_s = 180^\circ - \theta_i$. In the second case, the backscatter direction corresponds to a bistatic angle of either 180° or -180° , and the specular direction corresponds to a bistatic angle of 0° .

All these model comparisons will be discussed in order of seafloor type, beginning with rough rock and ending with silt. The seafloor types were chosen purely for illustration purposes. In reality, each type will consist of a wide range of subtypes

whose parameters may differ significantly from those used in this report. Thus the results given here should not be considered representative of these types of seafloors in general.

6.1 Rough Rock

Figure 4 compares the predictions of the older backscatter model [1] with those of the present model at a frequency of 20 kHz. For rough rock, the older backscatter prediction is purely empirical, and the approximate agreement between the older and newer models is a result of the fitting process described earlier. As noted by Ivakin and Jackson [11, 12], a surprising result of the inclusion of shear effects is that volume scattering becomes important for rocky seafloors and is expected, in fact, to be dominant for grazing angles smaller than the compressional critical angle (64.2°). Roughness scattering exhibits a minimum for grazing angles somewhat smaller than the shear critical angle (40.2°), while reflection loss (Eq. 25) reaches a peak in the same neighborhood. This is a Rayleigh wave effect [9] which provides a means of coupling energy into the rock. The volume scattering limitation of Eq. (42) produces a slight flattening of the angular dependence of scattering strength.

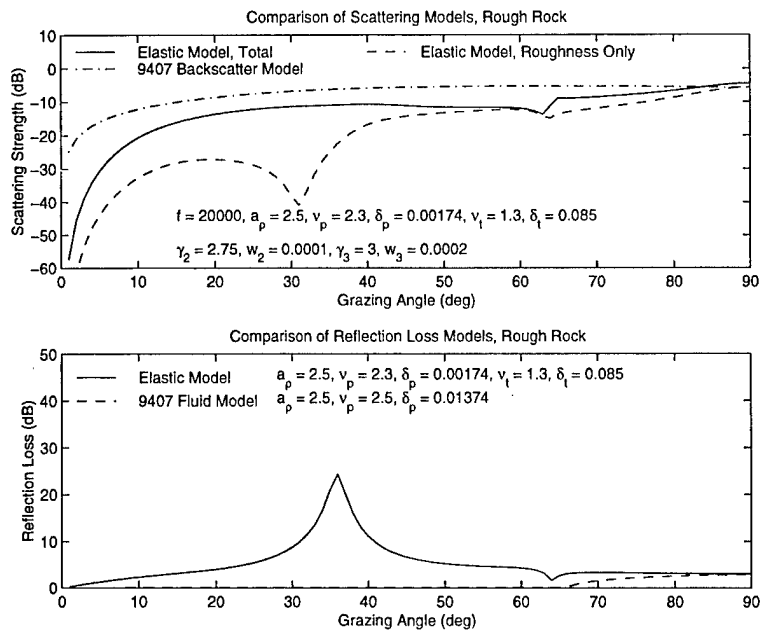


Figure 4: Comparison of predictions by the elastic and fluid scattering strength models and reflection loss model for backscattering at 20 kHz from rough rock.

The old and new reflection loss predictions are quite different. While the fluid model predicts negligible loss for grazing angles below the compressional critical angle,

the elastic model predicts substantial loss in this region. This behavior is in qualitative agreement with the conclusions of Keenan et al. [22], although no data are available from controlled experiments to check this prediction.

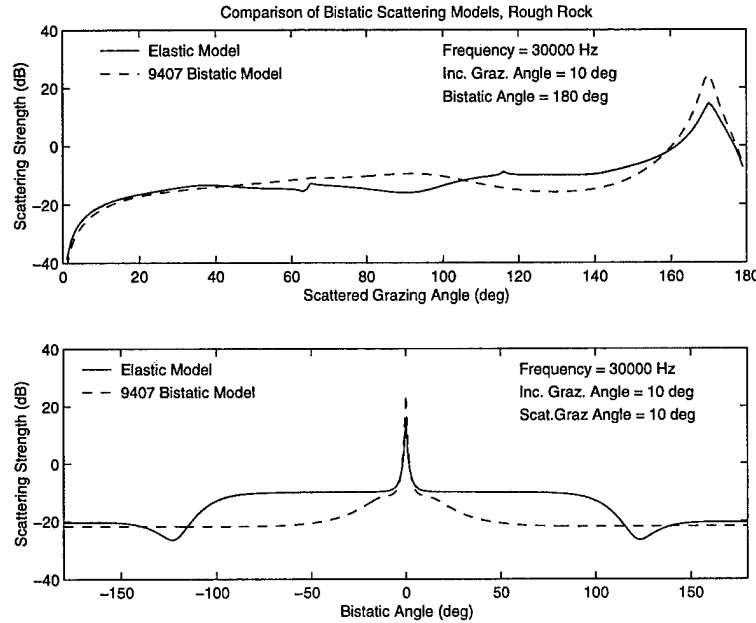


Figure 5: Comparison of predictions by the elastic and fluid bistatic scattering models at 30 kHz and a 10° incident grazing angle for rough rock.

Figures 5 and 6 compare predictions of the older and newer bistatic models for incident grazing angles of 10° and 45°, respectively. The newer model shows a narrow peak in the specular direction at the smaller (10°) incident grazing angle (Fig. 5). This peak is due to interface scattering and rises above a plateau owing to volume scattering. This plateau is limited to a value $10 \log_{10} \sigma_0 = -10$ dB by Eq. 42. While it seems safe to assert that volume scattering is important in this region, the predicted level and flat angular dependence seen in Fig. 5 are suspect owing to the ad hoc nature of Eq. 42.

6.2 Rock

The input parameters used for rock are the same as those used for rough rock except that the roughness and volume inhomogeneity levels are changed. The backscattering behavior (Fig. 7) and bistatic scattering behavior (Figs. 8 and 9) are similar to those for rough rock, while the reflection loss curve is identical.

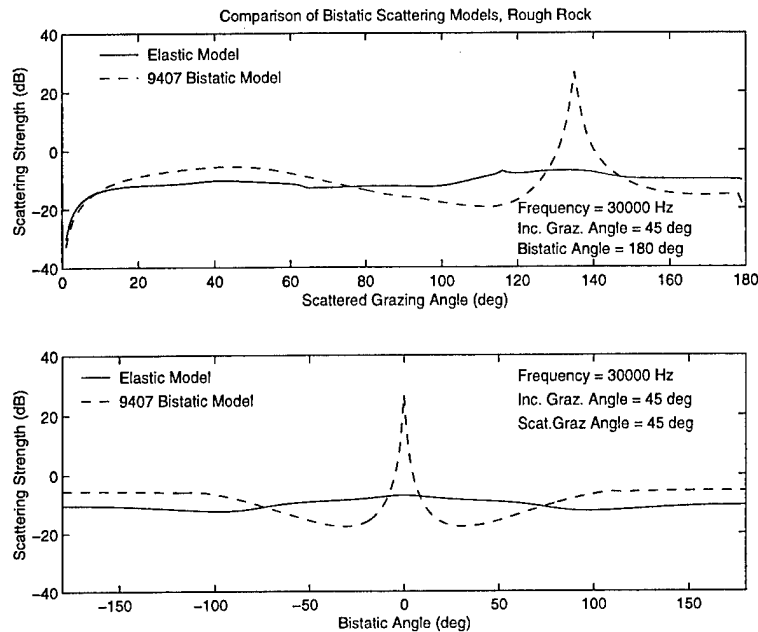


Figure 6: Comparison of predictions by the elastic and fluid bistatic scattering models at 30 kHz and a 45° incident grazing angle for rough rock.

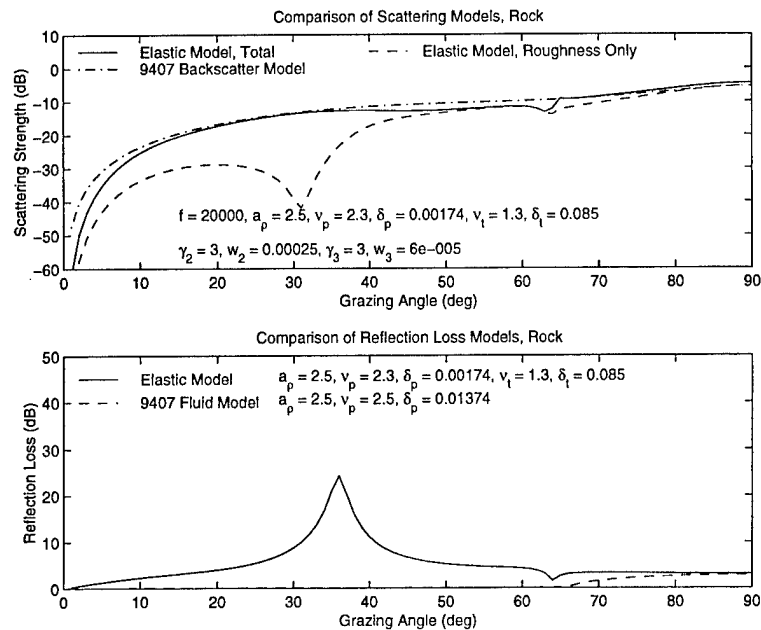


Figure 7: Comparison of predictions by the elastic and fluid scattering strength models and reflection loss model for backscattering at 20 kHz from rock.

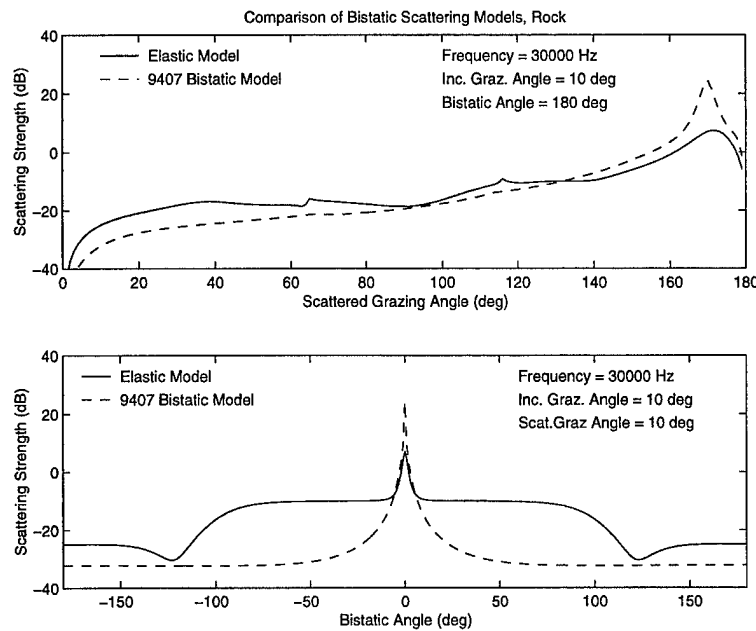


Figure 8: Comparison of predictions by the elastic and fluid bistatic scattering models at 30 kHz and a 10° incident grazing angle for rock.

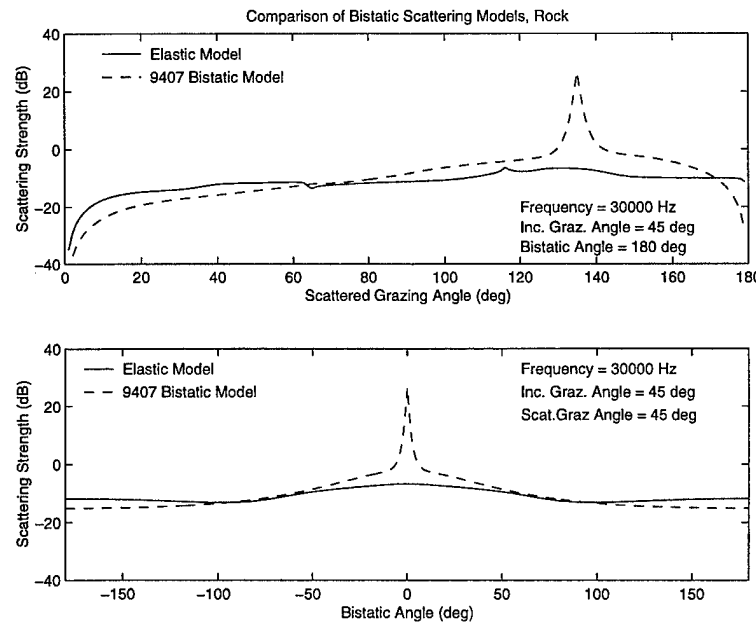


Figure 9: Comparison of predictions by the elastic and fluid bistatic scattering models at 30 kHz and a 45° incident grazing angle for rock.

6.3 Cobble

The density and compressional wave parameters for cobble were taken from Ref. [1] (compare parameters in Figs. 1 and 10), and the shear and roughness parameters were adjusted to fit the older backscatter model (Fig. 10). The resulting shear speed is slightly faster than the water sound speed. Unfortunately, no measured values are available for comparison. Volume scattering is relatively unimportant in this case, and the reflection loss of the new model is much larger than that of the fluid model described in Ref. [1]. The bistatic scattering behavior (Figs. 11 and 12) is similar to that for rock, with a narrow peak in the specular direction rising above a plateau of volume scattering. This plateau is narrower than in the rough rock and rock examples, indicating that the volume perturbation approximation is providing believable results over a larger angular regime.

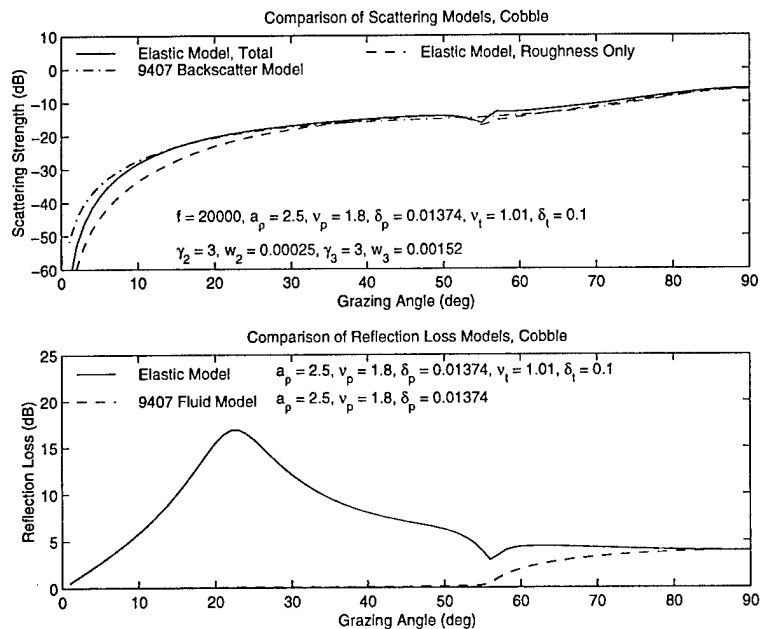


Figure 10: Comparison of predictions by the elastic and fluid scattering strength models and reflection loss model for backscattering at 20 kHz from cobble.

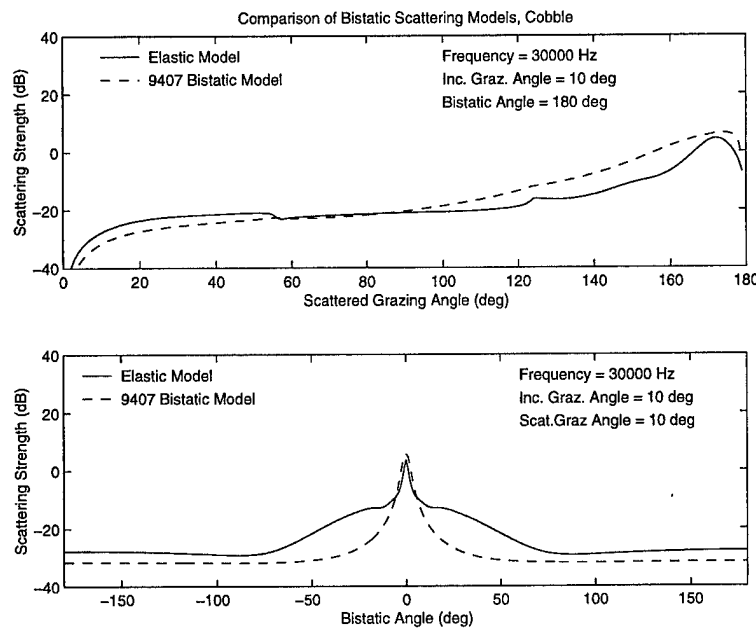


Figure 11: Comparison of predictions by the elastic and fluid bistatic scattering models at 30 kHz and a 10° incident grazing angle for cobble.

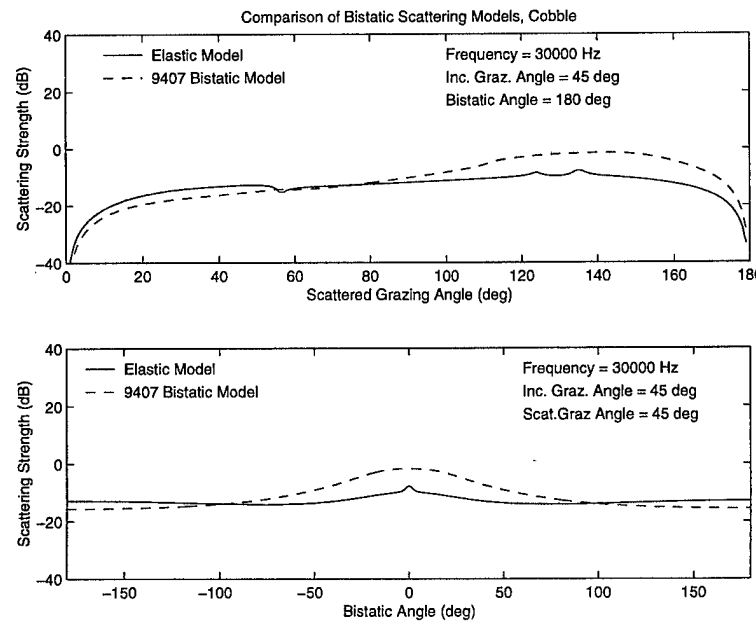


Figure 12: Comparison of predictions by the elastic and fluid bistatic scattering models at 30 kHz and a 45° incident grazing angle for cobble.

6.4 Sandy Gravel

For the sandy gravel example, all parameters except the roughness and shear parameters were taken from Ref. [1] using the default procedure defined earlier. Because data on shear waves in gravel were lacking, ν_t and δ_t were arbitrarily assigned values similar to those appropriate for coarse sand [23–26]. The two roughness parameters were assigned values from the older backscatter model. Figure 13 shows that the inclusion of shear increases the reflection loss somewhat for angles below the compressional critical angle (41.6°). The new model has essentially the same bistatic behavior as the older model of Ref. [1] (Figs. 14 and 15).

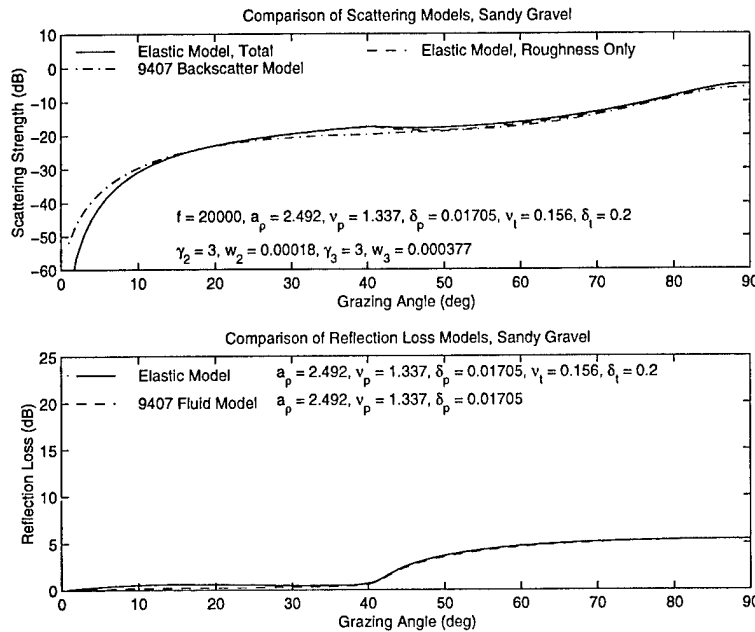


Figure 13: Comparison of predictions by the elastic and fluid scattering strength models and reflection loss model for backscattering at 20 kHz from sandy gravel.

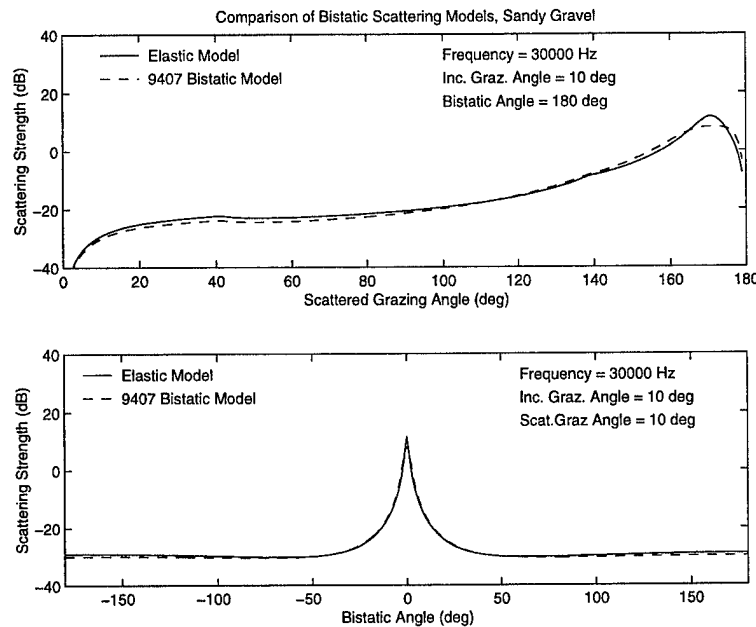


Figure 14: Comparison of predictions by the elastic and fluid bistatic scattering models at 30 kHz and a 10° incident grazing angle for sandy gravel.

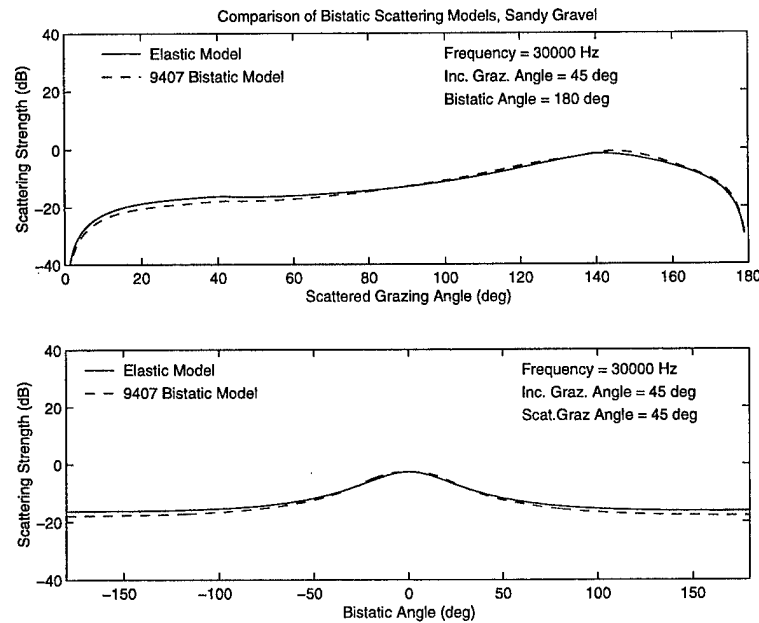


Figure 15: Comparison of predictions by the elastic and fluid bistatic scattering models at 30 kHz and a 45° incident grazing angle for sandy gravel.

6.5 Coarse Sand

The shear parameters for coarse sand were taken from Ivakin and Jackson [11] who, in turn, estimated their parameters from historical data [23, 24]. All other parameters were taken by default from Ref. [1]. As Figs. 16, 17, and 18 show, the reflection and bistatic behavior of the fluid and elastic models is essentially the same.

The older backscatter model gives larger scattering strengths at small grazing angles, owing to its use of composite roughness averaging. It has been suggested that composite roughness averaging may be rather poor for sands [4], but this issue requires further examination.

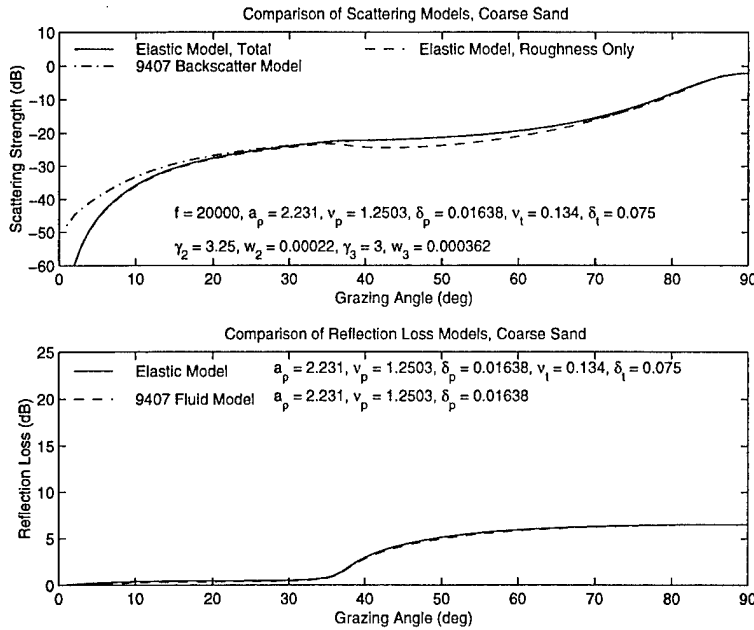


Figure 16: Comparison of predictions by the elastic and fluid scattering strength models and reflection loss model for backscattering at 20 kHz from coarse sand.

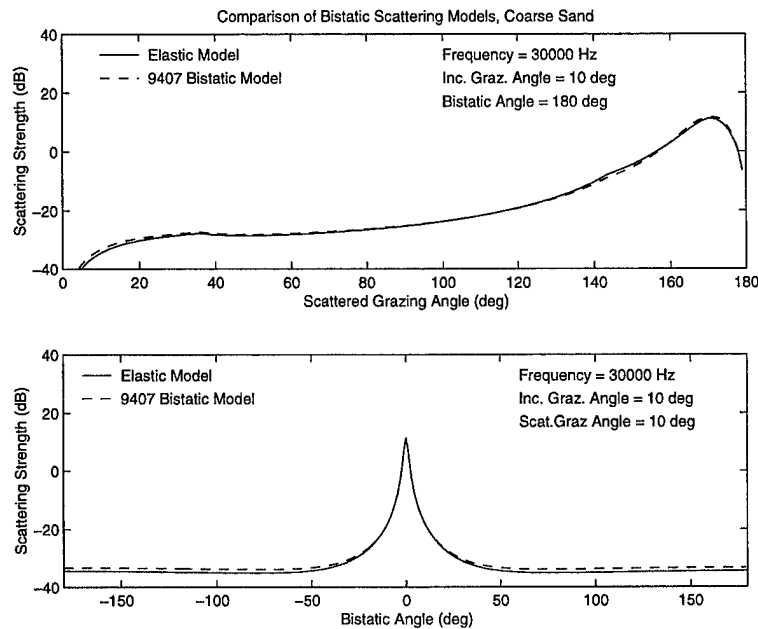


Figure 17: Comparison of predictions by the elastic and fluid bistatic scattering models at 30 kHz and a 10° incident grazing angle for coarse sand.

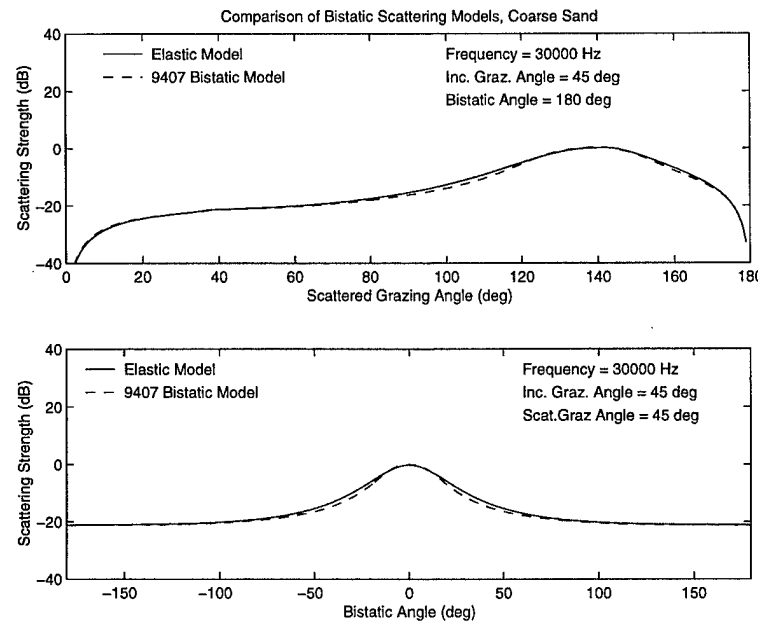


Figure 18: Comparison of predictions by the elastic and fluid bistatic scattering models at 30 Hz and a 45° incident grazing angle for coarse sand.

6.6 Medium and Fine Sand

For medium and fine sand all parameters were set by the default procedures, which render shear effects negligible. Not surprisingly, the predictions of the new model match those of the older models closely in all aspects: backscatter and reflection loss (Figs. 19 and 20) and bistatic scattering (Figs. 21–24).

While volume scattering is relatively unimportant for medium sand, it plays a substantial role for fine sand. The discrepancy between backscattering predictions by the old and new models at small grazing angles is rather small for fine sand owing to the lower level of roughness and the correspondingly small composite roughness averaging correction.

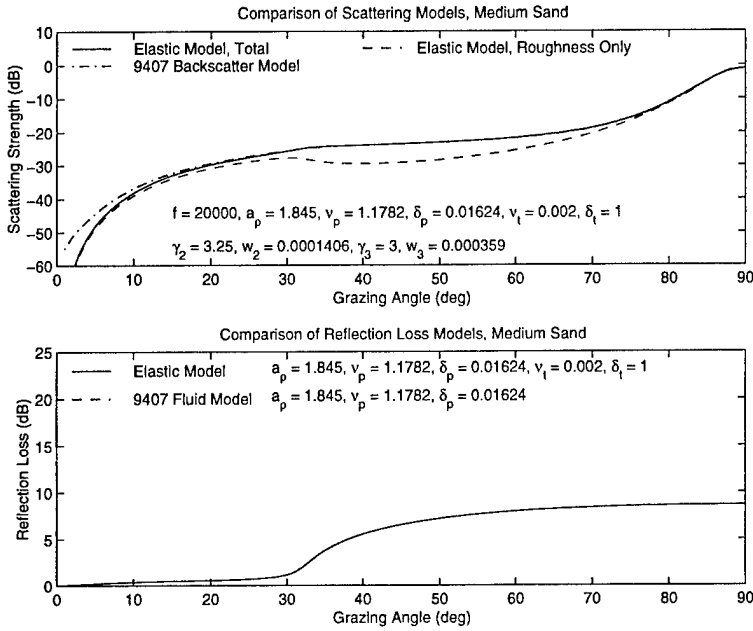


Figure 19: Comparison of predictions by the elastic and fluid scattering strength models and reflection loss model for backscattering at 20 kHz from medium sand.

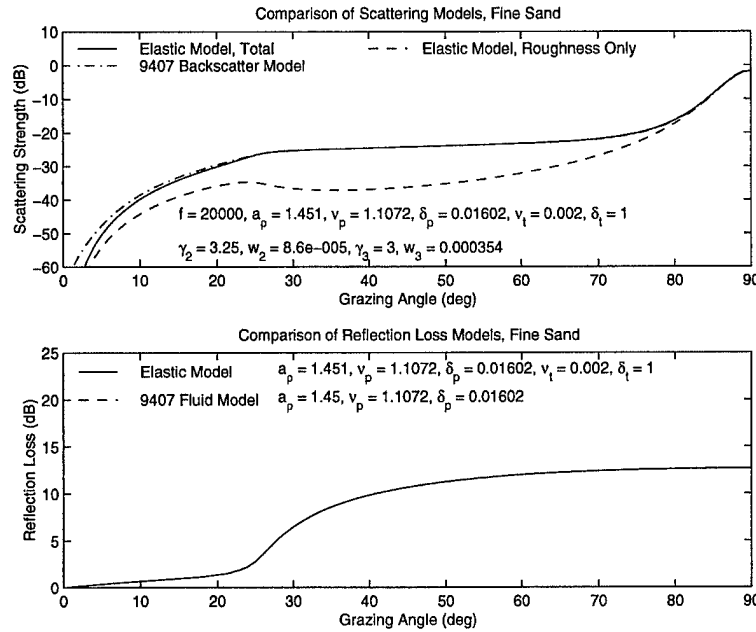


Figure 20: Comparison of predictions by the elastic and fluid scattering strength models and reflection loss model for backscattering at 20 kHz from fine sand.

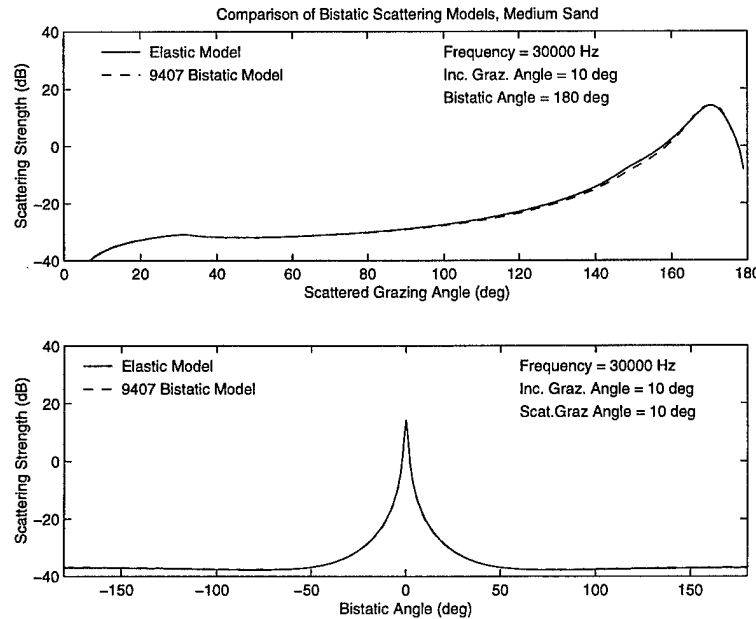


Figure 21: Comparison of predictions by the elastic and fluid bistatic scattering models at 30 kHz and a 10° incident grazing angle for medium sand.

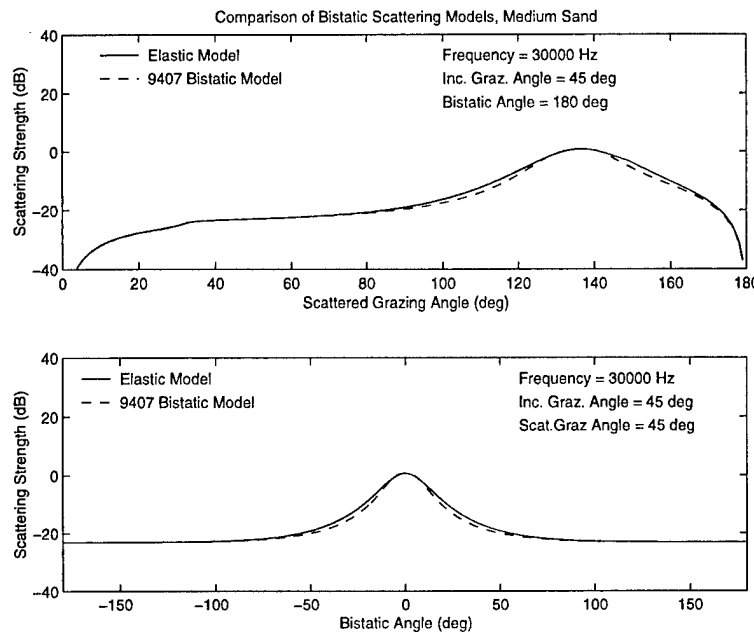


Figure 22: Comparison of predictions by the elastic and fluid bistatic scattering models at 30 kHz and a 45° incident grazing angle for medium sand.

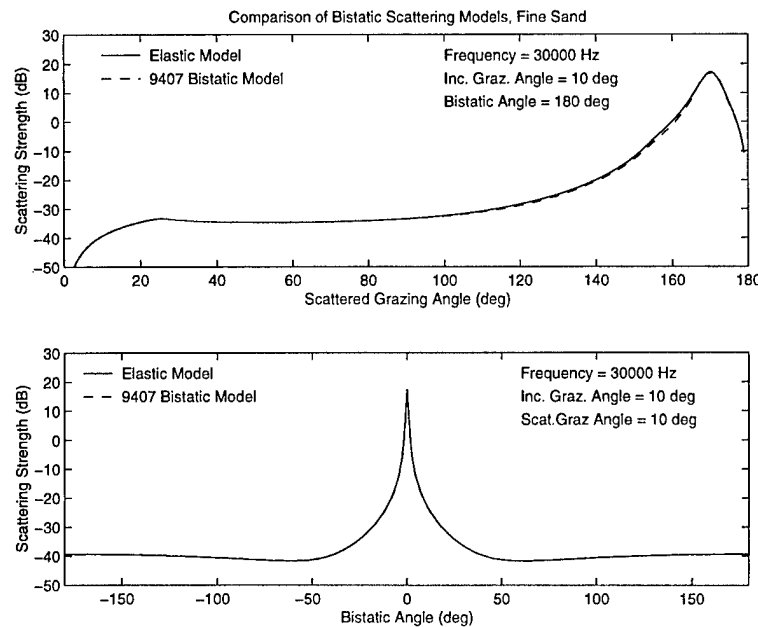


Figure 23: Comparison of predictions by the elastic and fluid bistatic scattering models at 30 kHz and a 10° incident grazing angle for fine sand.

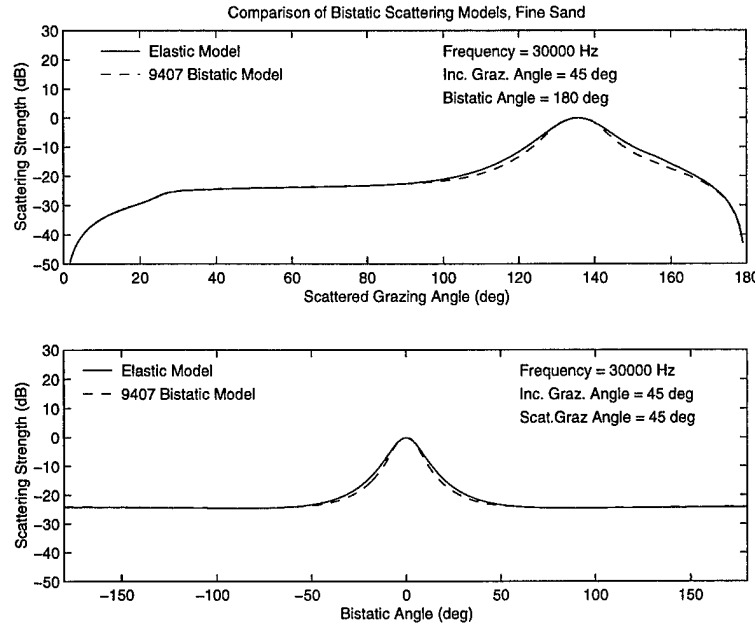


Figure 24: Comparison of predictions by the elastic and fluid bistatic scattering models at 30 kHz and a 45° incident grazing angle for fine sand.

6.7 Silt

Again, shear effects are ignored, and the parameters are taken from Ref. [1] using the default procedures. This is an example of a “slow” sediment for which volume scattering dominates except near normal incidence for backscattering and near the specular direction for bistatic scattering. In all cases, the elastic model is nearly indistinguishable from the older fluid models (Figs. 25–27).

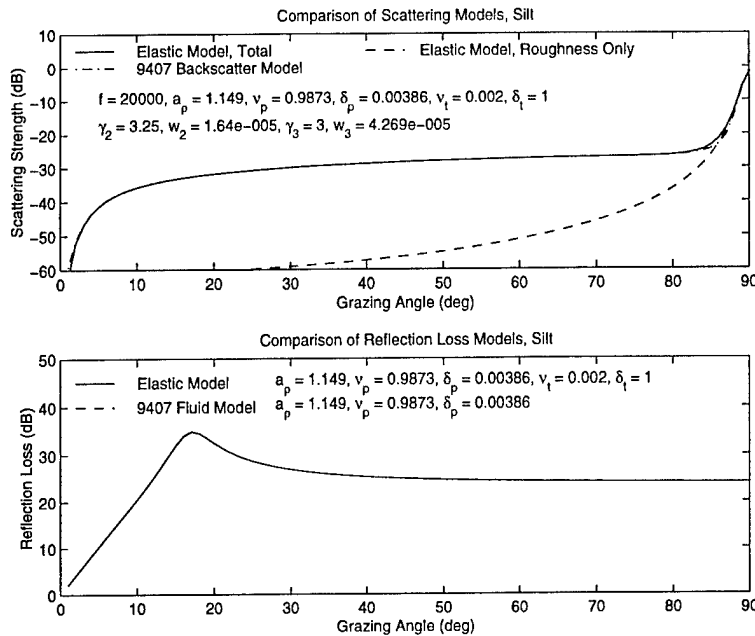


Figure 25: Comparison of predictions by the elastic and fluid scattering strength models and reflection loss model for backscattering at 20 kHz from silt.

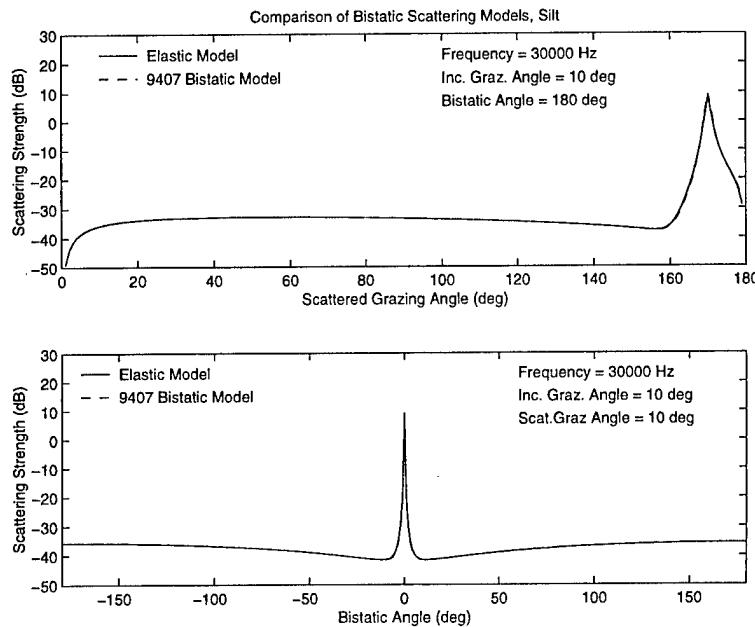


Figure 26: Comparison of predictions by the elastic and fluid bistatic scattering models at 30 kHz and a 10° incident grazing angle for silt.

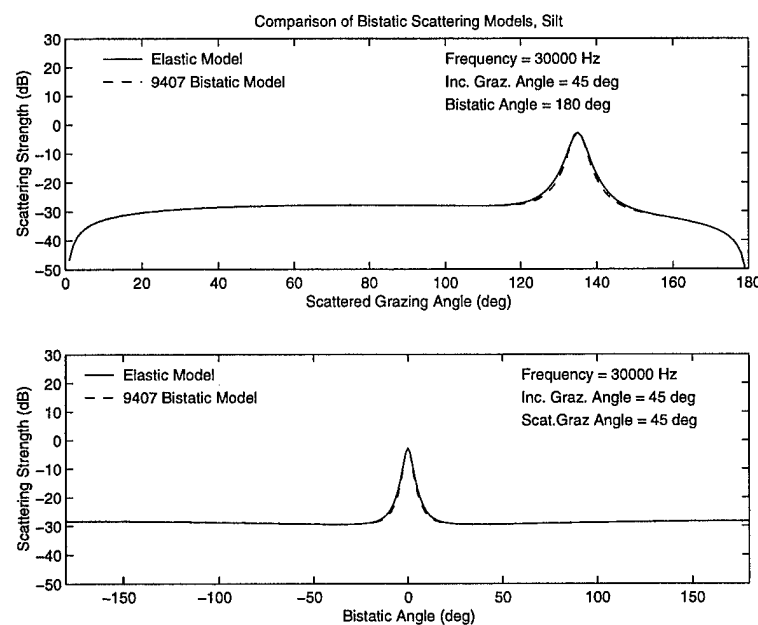


Figure 27: Comparison of predictions by the elastic and fluid bistatic scattering models at 30 kHz and a 45° incident grazing angle for silt.

7. CONCLUSIONS

The elastic scattering model combines the best features of three older fluid models (for backscattering, reflection, and bistatic scattering) in a single model and treats a wider range of seafloor types. It matches the older models in the regime where they are well tested, but experimental tests are needed for the extreme seafloor types, rock and very coarse-grained material (cobble and gravel). In particular, the unusual prediction that volume scattering is important in rock should be examined closely. In addition to such experimental tests, mathematical tests are needed for these same cases to determine the accuracy of the small-slope and volume perturbation approximations. It is clear that the volume perturbation approximation sometimes fails near the specular direction for the parameters used here for rough rock and rock.

REFERENCES

- [1] APL-UW High-Frequency Ocean Environmental Acoustic Models Handbook, Ch. IV, Bottom, APL-UW TR 9407, October 1994.
- [2] D. R. Jackson, D. P. Winebrenner, and A. Ishimaru, "Application of the composite roughness model to high-frequency bottom backscattering," *J. Acoust. Soc. Am.*, **79**, 1410–1422, 1986.
- [3] P. D. Mourad and D. R. Jackson, "High frequency sonar equation models for bottom backscatter and forward loss," *Proceedings OCEANS '89*, **4**, 1168–1175, 1989.
- [4] D. R. Jackson and K. B. Briggs, "High-frequency bottom backscattering: Roughness vs. sediment volume scattering," *J. Acoust. Soc. Am.*, **92**, 962–977, 1992.
- [5] D. R. Jackson, "Models for scattering from the sea bed," *Proc. Inst. Acoust.*, **16**, 161–169, 1994.
- [6] D. R. Jackson, K. B. Briggs, K. L. Williams, and M. D. Richardson, "Tests of models for high-frequency seafloor backscatter," *IEEE J. Oceanic Engr.*, **21**, 458–470, 1996.
- [7] K. L. Williams and D. R. Jackson, Bistatic Bottom Scattering: Model, Experiments, and Model/Data Comparison, APL-UW TR 9602, 1996.
- [8] K. L. Williams and D. R. Jackson "Bottom bistatic scattering: Experimental results and model comparison for a carbonate sediment," in *High Frequency Acoustics in Shallow Water*, edited by N.G. Pace, E. Pouliquen, O. Bergem, and A.P. Lyons, 601–605 (SACLANTCEN Conf. Proc. Series CP-45, NATO SACLANT Undersea Research Centre, La Spezia, Italy, 1997).
- [9] T. Yang and S. L. Broschat, "Acoustic scattering from a fluid-elastic-solid interface using the small slope approximation," *J. Acoust. Soc. Am.*, **96**, 1796–1803, 1994.
- [10] H.-H. Essen, "Scattering from a rough sedimental seafloor containing shear and layering," *J. Acoust. Soc. Am.*, **95**, 1299–1310, 1994.
- [11] A. N. Ivakin and D. R. Jackson, "Effects of shear elasticity on sea bed scattering: Numerical examples," *J. Acoust. Soc. Am.*, **103**, 346–354, 1998.
- [12] D. R. Jackson and A. N. Ivakin, "Scattering from elastic sea beds: First-order theory," *J. Acoust. Soc. Am.*, **103**, 336–345, 1998.
- [13] A. G. Voronovich, *Wave Scattering from Rough Surfaces* (Springer-Verlag, Berlin, 1994).
- [14] D. Wurmser, "A manifestly reciprocal theory of scattering in the presence of elastic media," *J. Math. Phys.* **37**, pp. 4434–4479, 1996.

- [15] J. E. Moe and D. R. Jackson, "First-order perturbation solution for rough surface scattering cross section including the effect of gradients," *J. Acoust. Soc. Am.*, **96**, 1748–1754, 1994.
- [16] A. N. Ivakin, "Sound scattering by inhomogeneities of an elastic half-space," *Soviet Physics-Acoustics*, **36**(4), 377–380, 1990.
- [17] T. Yamamoto, "Velocity variabilities and other physical properties of marine sediments measured by crosswell acoustic tomography," *J. Acoust. Soc. Am.*, **98**, 2235–2248, 1995.
- [18] T. Yamamoto, "Acoustic scattering in the ocean from velocity and density fluctuations in the sediments," *J. Acoust. Soc. Am.*, **99**, 866–879, 1996.
- [19] L. M. Brekhovskikh and Yu. P. Lysanov, *Fundamentals of Ocean Acoustics* (Springer-Verlag, Berlin, 1991).
- [20] W. A. Kuperman and H. Schmidt, "Rough surface elastic wave scattering in a horizontally stratified ocean," *J. Acoust. Soc. Am.*, **79**, 1767–1777, 1986.
- [21] D. K. Dacol and D. H. Berman, "Sound scattering from a randomly rough fluid-solid interface," *J. Acoust. Soc. Am.*, **84**, 292–302, 1988.
- [22] R. E. Keenan and H. Weinberg, Modeling the 1994 SOCAL Range's Northwest Quadrant Shallow-Water Torpedo Reverberation Data with the Comprehensive Acoustic System Simulation, Naval Undersea Warfare Center (NUWC)/Newport Technical Report 10496, 1 August 1995.
- [23] E. L. Hamilton, "Elastic properties of marine sediments," *J. Geophys. Res.*, **76**, 579–604, 1971.
- [24] E. L. Hamilton, "Attenuation of shear waves in marine sediments," *J. Acoust. Soc. Am.*, **60**, 334–338, 1976.
- [25] M. D. Richardson, E. Muzi, B. Miaschi, and F. Turgutcan, "Shear wave velocity gradients in near-surface marine sediment," in *Shear Waves in Marine Sediments*, J. M. Hovem, M. D. Richardson, and R. D. Stoll, Eds. (Kluwer, Dordrecht, 1991), pp. 295–304.
- [26] A. Barbagelata, M. Richardson, B. Miaschi, E. Muzi, P. Guerrini, L. Troiano, and T. Akal, "ISSAMS: An in situ sediment acoustic measurement system," in *Shear Waves in Marine Sediments*, edited by J. M. Hovem, M. D. Richardson, and R. D. Stoll, 305–312 (Kluwer, Dordrecht, 1991).

REPORT DOCUMENTATION PAGE

*Form Approved
OPM No. 0704-0188*

Public reporting burden for this collection of information is estimated to average 1 hour per response, including the time for reviewing instructions, searching existing data sources, gathering and maintaining the data needed, and reviewing the collection of information. Send comments regarding this burden estimate or any other aspect of this collection of information, including suggestions for reducing this burden, to Washington Headquarters Services, Directorate for Information Operations and Reports, 1215 Jefferson Davis Highway, Suite 1204, Arlington, VA 22202-4302, and to the Office of Information and Regulatory Affairs, Office of Management and Budget, Washington, DC 20503.

1. AGENCY USE ONLY (Leave blank)	2. REPORT DATE	3. REPORT TYPE AND DATES COVERED	
4. TITLE AND SUBTITLE	High-Frequency Bistatic Scattering Model for Elastic Seafloors		
6. AUTHOR(S)	Darrell R. Jackson		
7. PERFORMING ORGANIZATION NAME(S) AND ADDRESS(ES)	Applied Physics Laboratory University of Washington 1013 NE 40th Street Seattle, WA 98105-6698		
9. SPONSORING / MONITORING AGENCY NAME(S) AND ADDRESS(ES)	Dr. Jeffrey Simmen (Code 321OA) Office of Naval Research Ballson Tower One 800 North Quincy Street Arlington, VA 22217-5660		
11. SUPPLEMENTARY NOTES			
12a. DISTRIBUTION / AVAILABILITY STATEMENT Approved for public release; distribution is unlimited.		12b. DISTRIBUTION CODE	
13. ABSTRACT (Maximum 200 words) A model for bistatic acoustic scattering at high frequencies (10–100 kHz) from elastic seafloors is developed by combining the elastic small-slope roughness scattering model of Yang and Broschat with the elastic volume scattering model of Ivakin. The combined model is applicable to a variety of seafloors, including clays, silts, sands, gravel, and rock. Although elastic effects are negligible in sands and finer sediments, they are essential in treating reflection and scattering by rock, which cannot be usefully represented by a fluid model. Use of the small-slope approximation makes it possible to avoid the cumbersome interpolation between the Kirchhoff and perturbation approximations employed in the previous APL-UW backscattering model and allows larger levels of roughness than are permitted with conventional scattering approximations. The model results agree with those of the APL-UW backscattering model and with those of the APL-UW bistatic model for clays, silts, and sands. The inclusion of elastic effects attributes the high levels of scattering observed for cobble and rock seafloors to a combination of roughness and volume scattering, and replaces the empirical treatment of cobble and rock seafloors previously used in the APL-UW backscattering model by a physical one. For these cases, the new model sometimes produces unphysical results for scattering near the specular direction, indicating the need for further work on this problem.			
14. SUBJECT TERMS Reverberation, Bottom acoustic scattering, Bottom loss, Small slope approximation		15. NUMBER OF PAGES 44	
		16. PRICE CODE	
17. SECURITY CLASSIFICATION OF REPORT Unclassified	18. SECURITY CLASSIFICATION OF THIS PAGE Unclassified	19. SECURITY CLASSIFICATION OF ABSTRACT Unclassified	20. LIMITATION OF ABSTRACT SAR